Eur. Phys. J. A (2015) **51**: 161
DOI 10.1140/epja/i2015-15161-5

THE EUROPEAN PHYSICAL JOURNAL A

Regular Article – Theoretical Physics

Simultaneous distribution between the deflection angle and the lateral displacement under the Molière theory of multiple scattering

Takao Nakatsuka[1,a,b], Kazuhide Okei[2], Atsushi Iyono[3], and Alex F. Bielajew[4]

[1] Laboratory of Information Science, Okayama Shoka University, Okayama 700-8601, Japan
[2] Dept. of Information Sciences, Kawasaki Medical School, Kurashiki 701-0192, Japan
[3] Dept. of Fundamental Science, Faculty of Science, Okayama university of Science, Okayama 700-0005, Japan
[4] Dept. Nuclear Engineering and Radiological Sciences, Univ. of Michigan, Ann Arbor, MI 48109-2104, USA

Received: 3 November 2015
Published online: 22 December 2015 –
Communicated by M. Anselmino

Abstract. Simultaneous distribution between the deflection angle and the lateral displacement of fast charged particles traversing through matter is derived by applying numerical inverse Fourier transforms on the Fourier spectral density solved analytically under the Molière theory of multiple scattering, taking account of ionization loss. Our results show the simultaneous Gaussian distribution at the region of both small deflection angle and lateral displacement, though they show the characteristic contour patterns of probability density specific to the single and the double scatterings at the regions of large deflection angle and/or lateral displacement. The influences of ionization loss on the distribution are also investigated. An exact simultaneous distribution is derived under the fixed energy condition based on a well-known model of screened single scattering, which indicates the limit of validity of the Molière theory applied to the simultaneous distribution. The simultaneous distribution will be valuable for improving the accuracy and the efficiency of experimental analyses and simulation studies relating to charged particle transports.

1 Introduction

Molière's theory of multiple scattering [1–3] is still a most advanced theory, taking account of the single and the plural scatterings together in his theory, and showing rapid convergence reflecting expansion by the low-frequent large-angle scattering [4]. Nevertheless, no distributions other than those of the deflection angle, the lateral displacement, and the linear combination of the both, were indicated by him [5], due to the mathematical difficulty or complexity.

Effective approaches have been attempted to apply the Molière theory to other problems. A differentially formulated Molière theory was developed by Kamata and Nishimura, expressing Molière's theory by a simple ordinary differential equation for the Fourier spectral density, introducing new physical constants [6, 7]. They indicated the terms appended by the Molière theory to their structure functions of electromagnetic shower. Later, the formulation was applied by Nakatsuka to evaluate corrections by the Molière theory to the longitudinal distribution of fast charged particles traversing through matter [8] and by Nakatsuka and Nishimura to derive the angular and the lateral distributions of those particles under the Molière theory with ionization [4]. On the other hand, the numerical functional transform was applied by Andreo *et al.* to derive the higher-order terms of Molière's series-coefficient function [9, 10], as well as by Bielajew to derive the exact angular distribution based on a model of screened single scattering [11, 12].

We derive the simultaneous distribution between the deflection angle and the lateral displacement, not solved yet under the Molière theory [13], by applying the above effective methods. The Molière simultaneous distribution determines the energy of charged particle more accurately with the maximum likelihood method than the Molière individual distribution for the deflection angle [14]. The former will give more reliable results than the latter in experimental analyses concerning charged particle transports, *e.g.* momentum measurements by emulsion cloud chambers [15,16] or streamer tube chambers [17,18] in neutrino-oscillation experiments, as well as arrival-direction decisions in astronomical cosmic-ray observations [19, 20].

Practically, we acquire the simultaneous distribution with ionization by applying the inverse Fourier transforms

[a] e-mail: nakatuka@olive.plala.or.jp
[b] Retired now from the university.

numerically on the Fourier spectral density solved analytically by the Molière theory of differential formulation. The distribution expressed by a power series of rapid convergence is also presented. The results indicated by contour maps of the probability density show characteristic patterns of the single and the double scatterings other than the central Gaussian pattern. We also propose a mathematically exact simultaneous distribution based on a well-known model of screened single scattering [11,12], under the fixed energy condition. Comparing the results with those derived by the Molière theory, we discuss the limits of validity and applicability of the Molière theory to the simultaneous distribution.

2 Molière simultaneous distribution between the deflection angle and the lateral displacement

2.1 The analytical solution of Fourier spectral density for the simultaneous distribution

Let $F(\vec{\chi},\vec{r},t)\,\mathrm{d}\vec{\chi}\,\mathrm{d}\vec{r}$ be the simultaneous distribution between the deflection angle $\vec{\chi}\equiv(\theta_y,\theta_z)$ and the lateral displacement $\vec{r}\equiv(y,z)$ of fast charged particles after penetrating a matter of the thickness t, with $\vec{r}$ and t measured in units of radiation length X_0 [21]. Then the diffusion equation is described as [4,11]

$$\frac{\partial}{\partial t}F(\vec{\chi},\vec{r},t)=-\vec{\chi}\,\frac{\partial F(\vec{\chi},\vec{r},t)}{\partial\vec{r}}+\iint\left\{F\left(\vec{\chi}-\vec{\chi'},\vec{r},t\right)-F(\vec{\chi},\vec{r},t)\right\}\sigma(\chi')\,\mathrm{d}\vec{\chi'},\tag{1}$$

where $\sigma(\chi)$ denotes the screened single-scattering cross-section for charged particles of energy E under the small angle approximation [13],

$$\sigma(\chi)2\pi\chi\,\mathrm{d}\chi\,\mathrm{d}t=\frac{1}{\pi\Omega}\frac{K^2}{E^2}\chi^{-4}2\pi\chi\,\mathrm{d}\chi\,\mathrm{d}t,\quad\text{for}\quad\chi>\sqrt{e}\chi_a,\tag{2}$$

with the characteristic screening angle [1,3] of

$$\chi_a=(K/E)/e^{(\Omega-1+2C)/2},\tag{3}$$

K and Ω denote the scattering constants specific to the matter introduced by Kamata and Nishimura [4,6,7], and $C=0.57721\ldots$, denotes Euler's constant. We derive the simultaneous distribution, taking account of continuous energy loss by ionization with

$$E=E_0-\varepsilon t,\tag{4}$$

where E_0 denotes the incident energy and ε the critical energy [4,21]. Applying Fourier transforms,

$$\tilde{F}(\vec{\zeta},\vec{\eta},t)=\frac{1}{4\pi^2}\iiint e^{i\vec{\zeta}\vec{\chi}+i\vec{\eta}\,\vec{r}}F(\vec{\chi},\vec{r},t)\,\mathrm{d}\vec{\chi}\,\mathrm{d}\vec{r},\tag{5}$$

we have a diffusion equation for the Fourier spectral density,

$$\begin{aligned}\frac{\partial\tilde{F}}{\partial t'}&=\vec{\eta}\frac{\partial\tilde{F}}{\partial\vec{\zeta'}}+2\pi\tilde{F}\int_0^\infty\{J_0(\zeta'\chi)-1\}\,\sigma(\chi)\chi\,\mathrm{d}\chi\\&=\vec{\eta}\frac{\partial\tilde{F}}{\partial\vec{\zeta'}}-\frac{K^2\zeta'^2}{4E'^2}\tilde{F}\left\{1-\frac{1}{\Omega}\ln\frac{K^2\zeta'^2}{4E'^2}\right\},\end{aligned}\tag{6}$$

according to the differentially formulated Molière theory [4,6,7], where $\vec{\zeta}\equiv(\zeta_y,\zeta_z)$ and $\vec{\eta}\equiv(\eta_y,\eta_z)$ denote the Fourier variables corresponding to $\vec{\chi}$ and $\vec{r}$, respectively. Note that the variables $\vec{\zeta'}$ and E' change together with the increase of variable t'. The differential term with $\vec{\zeta'}$ vanishes when we replace the variable $\vec{\zeta'}$ by

$$\vec{\zeta'}=\vec{\zeta}+(t-t')\vec{\eta},\tag{7}$$

where t and $\vec{\zeta}$ denote thickness and Fourier variable at the destination, so that eq. (6) is integrated as [4]

$$\begin{aligned}\ln 4\pi^2\tilde{F}&=-\int_0^t\frac{K^2(\vec{\zeta}+(t-t')\vec{\eta})^2}{4(E_0-\varepsilon t')^2}\\&\quad\times\left\{1-\frac{1}{\Omega}\ln\frac{K^2(\vec{\zeta}+(t-t')\vec{\eta})^2}{4(E_0-\varepsilon t')^2}\right\}\mathrm{d}t'\\&=\int_0^1\frac{\theta_{\mathrm{M}}^2E_0E(\vec{\zeta}+\vec{\eta}tu)^2}{4B(E+\varepsilon tu)^2}\ln\frac{\theta_{\mathrm{M}}^2E_0E(\vec{\zeta}+\vec{\eta}tu)^2}{4e^B(E+\varepsilon tu)^2}\,\mathrm{d}u,\end{aligned}\tag{8}$$

where u replaces $(t-t')/t$, E denotes the destination energy at t, and B and θ_{M}, called as *the expansion parameter* and *the scale angle* [4], are introduced as

$$B-\ln B=\Omega-\ln\Omega+\ln t,\tag{9}$$

$$\theta_{\mathrm{M}}^2=(B/\Omega)K^2t/(E_0E).\tag{10}$$

The thickness t and the square of scale angle θ_{M}^2 divided by $K^2/(E_0E)$ for charged particles traversing through matters of H_2O ($\Omega=15.2$, $K=19.1\,\mathrm{MeV}$), Fe ($\Omega=14.3$, $K=19.8\,\mathrm{MeV}$), and Pb ($\Omega=13.0$, $K=20.7\,\mathrm{MeV}$) are plotted against B in figs. 1 and 2, respectively.

By taking the spectral density $\tilde{F}(\vec{\zeta},\vec{\eta},t)$ of eq. (5) on the coordinates of $\vec{\zeta}=(\zeta,0)$ and $\vec{\eta}=(\eta,0)$, we have the spectral density for the projected components, as

$$\tilde{f}(\zeta,\eta t,t)=\frac{1}{2\pi}\exp\left[\int_0^1\frac{\theta_{\mathrm{M}}^2E_0E(\zeta+\eta tu)^2}{4B(E+\varepsilon tu)^2}\times\ln\frac{\theta_{\mathrm{M}}^2E_0E(\zeta+\eta tu)^2}{4e^B(E+\varepsilon tu)^2}\,\mathrm{d}u\right].\tag{11}$$

We expressed the spectral density as the function of ζ and ηt. Then applying the inverse Fourier transforms with ζ and ηt, we have the simultaneous distribution between the projected components, θ and y, as

$$f(\theta,\psi,t)\,\mathrm{d}\theta\,\mathrm{d}\psi=\frac{\mathrm{d}\theta\,\mathrm{d}(y/t)}{2\pi}\int_{-\infty}^\infty\int_{-\infty}^\infty e^{-i\theta\zeta-i\psi(\eta t)}\times\tilde{f}(\zeta,\eta t,t)\,\mathrm{d}\zeta\,\mathrm{d}(\eta t),\tag{12}$$

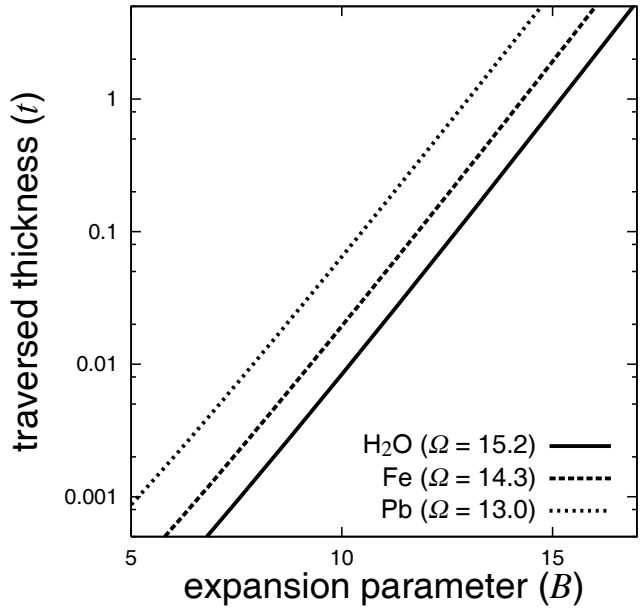

Fig. 1. The traversed thickness t in units of radiation length plotted against B for matters of H_2O, Fe, and Pb.

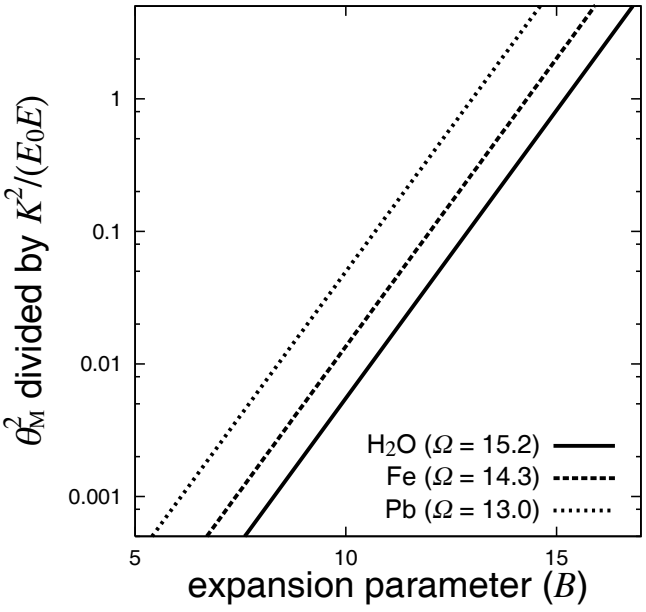

Fig. 2. The squared scale angle $\theta_{\rm M}^2$ divided by $K^2/(E_0E)$ plotted against B for matters of H_2O, Fe, and Pb.

where we expressed the simultaneous distribution as the function of the deflection angle θ and the chord-angle ψ, defined as

$$\psi \equiv y/t. \tag{13}$$

It should be reminded that the variables ζ and ηt always appear in the forms of $\theta_{\rm M}\zeta$ and $\theta_{\rm M}\eta t$ in the Fourier spectral density of eq. (11), so that the variables θ and ψ become scaled by $\theta_{\rm M}$ in the probability density of $f(\theta,\psi,t)$ due to the relation of eq. (12).

Note that the diffusion equation (1) is valid under the small angle approximation [13] where θ^2 is required smaller enough than 1. Thus so as the Molière simultaneous distributions derived below to be valid, $\theta_{\rm M}^2$ which increases with t (or the corresponding B) and works proportionally to $K^2/(E_0E)$ is required smaller enough than 1. Note also that the continuous energy loss of eq. (4) is valid for charged particles not to suffer radiation loss, *e.g.* for electrons with their energies of about $E < \varepsilon$ [21] and for muons with their energies of about $E < 625\,\mathrm{GeV}$ in the standard rock [22].

2.2 Double Fourier transforms to derive the simultaneous distribution

The simultaneous distribution is derived by the double Fourier transforms of eq. (12), by applying FFT (Fast Fourier Transform) tools [23] or applying numerical functional transforms. As it holds a symmetric relation of

$$\tilde{f}(-\zeta,-\eta t,t) = \tilde{f}(\zeta,\eta t,t), \tag{14}$$

the double Fourier transforms of eq. (12) is reduced to the double cosine transforms as

$$f(\theta,\psi,t)\,\mathrm{d}\theta\,\mathrm{d}\psi = \frac{\mathrm{d}\theta\,\mathrm{d}(y/t)}{\pi}\int_0^\infty \mathrm{d}(\eta t)\int_{-\infty}^\infty \cos(\theta\zeta+\psi\eta t) \times\tilde{f}(\zeta,\eta t,t)\,\mathrm{d}\zeta. \tag{15}$$

The simultaneous distribution can also be expressed as $g(\rho,\varphi,t)\rho\,\mathrm{d}\rho\,\mathrm{d}\varphi$ in the cylindrical coordinate, satisfying

$$f(\theta,\psi,t) = g(\rho,\varphi,t), \tag{16}$$

with

$$\theta = \rho\cos\varphi, \qquad \psi = \rho\sin\varphi. \tag{17}$$

On the radial axis with the azimuthal angle of 0, the probability density is expressed as

$$g(\rho,0,t) = f(\rho,0,t) = \frac{1}{\pi}\int_0^\infty \mathrm{d}\zeta\cos(\rho\zeta) \times\int_{-\infty}^\infty \tilde{f}(\zeta,\eta t,t)\,\mathrm{d}(\eta t). \tag{18}$$

If we introduce the new θ'-ψ' and ζ'-$\eta' t$ coordinates by rotating both the θ-ψ and ζ-ηt coordinates with φ, the probability density on the θ' axis, or $g(\rho,\varphi,t)$, is derived same way as eq. (18) on the rotated coordinate,

$$g(\rho,\varphi,t) = \frac{1}{\pi}\int_0^\infty \mathrm{d}\zeta'\cos(\rho\zeta') \times\int_{-\infty}^\infty \tilde{f}(\zeta'\cos\varphi-\eta' t\sin\varphi,\zeta'\sin\varphi+\eta' t\cos\varphi,t)\,\mathrm{d}(\eta' t). \tag{19}$$

2.3 The simultaneous distribution under the Gaussian approximation

Integrating eq. (11) with the limiting condition of $B\to\infty$, we have the analytical solution of simultaneous spectral

density under the Gaussian approximation [13], as

$$\tilde{f}_{\rm G}(\zeta,\eta t,t) = \frac{1}{2\pi}\exp\left[-\int_0^1 \frac{\theta_{\rm M}^2 E_0 E(\zeta+\eta t u)^2}{4(E+\varepsilon t u)^2}\,{\rm d}u\right]$$
$$= \frac{1}{2\pi}\exp\left[-\frac{\theta_{\rm M}^2 E_0 E}{4\varepsilon^2 t^2}\left\{\eta^2 t^2 - \frac{2\eta t(E\eta t-\varepsilon t\zeta)}{\varepsilon t}\right.\right.$$
$$\left.\left.\times\ln\frac{E_0}{E} + \frac{(E\eta t-\varepsilon t\zeta)^2}{E_0 E}\right\}\right], \qquad (20)$$

so that we have the Gaussian simultaneous distribution

$$f_{\rm G}(\theta,\psi,t)\,{\rm d}\theta\,{\rm d}\psi = \frac{\varepsilon^2 t^2/(E_0E)}{\left\{\varepsilon^2 t^2/(E_0E) - \ln^2(E_0/E)\right\}^{1/2}}\frac{{\rm d}\theta\,{\rm d}\psi}{\pi\theta_{\rm M}^2}$$
$$\times\exp\left[-\frac{\varepsilon^2 t^2/(E_0E)/\theta_{\rm M}^2}{\varepsilon^2 t^2/(E_0E) - \ln^2(E_0/E)}\right.$$
$$\times\left\{\theta^2 - \frac{2\theta(E\theta+\varepsilon t\psi)}{\varepsilon t}\ln\frac{E_0}{E}\right.$$
$$\left.\left.+\ \frac{(E\theta+\varepsilon t\psi)^2}{E_0E}\right\}\right]. \qquad (21)$$

These spectral density and the distribution agree with Eyges' results [24], if we regard his $p\beta$ as our E.

Especially under the fixed energy condition, we have

$$\tilde{f}_{\rm G}(\zeta,\eta t,t) = \frac{1}{2\pi}\exp\left[-\frac{\theta_{\rm M}^2}{4}\left(\zeta^2+\zeta\eta t+\frac{\eta^2 t^2}{3}\right)\right], \quad (22)$$

at the limit of $\varepsilon\to 0$ thus $E_0\to E$, so that we have the simultaneous distribution

$$f_{\rm G}(\theta,\psi,t)\,{\rm d}\theta\,{\rm d}\psi =$$
$$\frac{2\sqrt{3}}{\pi\theta_{\rm M}^2}\exp\left[-\frac{4}{\theta_{\rm M}^2}\left(\theta^2-3\theta\psi+3\psi^2\right)\right]{\rm d}\theta\,{\rm d}\psi, \qquad (23)$$

well known as the Fermi distribution [21].

2.4 Molière simultaneous distribution under the fixed energy condition

Integrating eq. (11) with the limiting condition of $\varepsilon\to 0$, we have the analytical solution of simultaneous spectral density under the fixed energy condition, as

$$\ln 2\pi\tilde{f} =$$
$$\frac{1}{B}\frac{\theta_{\rm M}^2}{12\eta t}\left\{(\zeta+\eta t)^3\ln\frac{\theta_{\rm M}^2(\zeta+\eta t)^2}{4e^{2/3+B}} - \zeta^3\ln\frac{\theta_{\rm M}^2\zeta^2}{4e^{2/3+B}}\right\}, \qquad (24)$$

identical with Molière's result [5], where we should remind his $\chi_c'\sqrt{l_0 B}$ agrees with our $\theta_{\rm M}$.

By applying the double cosine transforms of eq. (15), we have the Molière simultaneous distribution $f(\theta,\psi,t)$ between the deflection angle θ and the chord-angle $\psi\equiv y/t$ as indicated in fig. 3 for $B=8$, where we find the probability density decreases as two-dimensional Gaussian at the central region of $\rho\ll\theta_{\rm M}$. The same distribution is also indicated in fig. 4 by the radial variation $g(\rho,\varphi,t)$ of the density defined in eq. (19), where we find the probability density decreases with power law of the index of about -4 or -6 at the peripheral regions of $\rho\gg\theta_{\rm M}$ depending on the azimuthal angle φ of the radial direction (the indexes of about -4.2, -3.9, -6.2, -6.1, -6.0, and -6.0 for φ of $\pi/6$, 0, $\pi/3$, $5\pi/6$, $\pi/2$, and $2\pi/3$, from the top line to the bottom). The probability density $f(\theta,\psi,t)$ is also indicated in the contour map in fig. 5, whose characteristic patterns appearing in the peripheral regions are discussed later in subsect. 3.3.

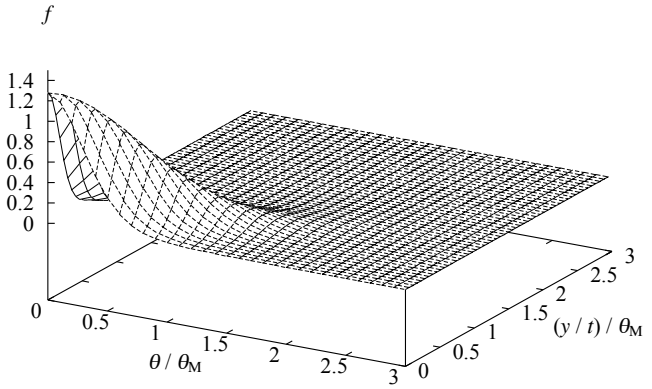

Fig. 3. Probability density of the Molière simultaneous distribution $f(\theta,\psi,t)$ between the deflection angle θ and the chord-angle $\psi\equiv y/t$ with the both projected angles scaled by $\theta_{\rm M}$, for $B=8$ under the fixed energy condition.

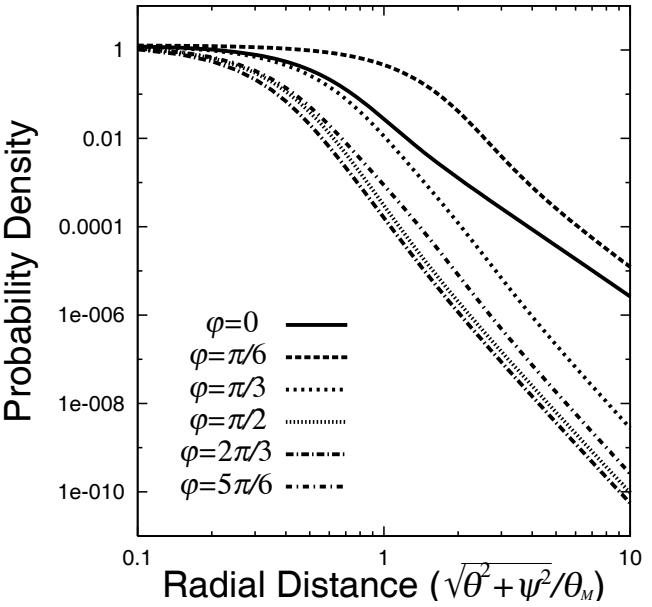

Fig. 4. Radial variation of the Molière simultaneous distribution $f(\theta,\psi,t)\equiv g(\rho,\varphi,t)$ for $B=8$ under the fixed energy condition with the radial distance scaled by $\theta_{\rm M}$, on the azimuthal angles φ of $\pi/6$, 0, $\pi/3$, $5\pi/6$, $\pi/2$, and $2\pi/3$ from top to bottom.

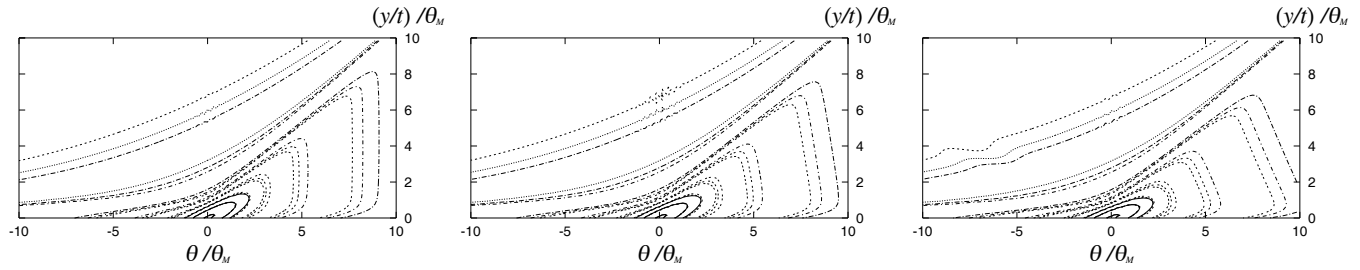

Fig. 5. Contour maps of the probability density of the Molière simultaneous distribution between the deflection angle θ and the chord-angle $\psi \equiv y/t$ with the both projected angles scaled by $\theta_{\rm M}$, in cases of fixed energy (left), as well as with fractional energy-loss of 1/4 (middle) and 1/2 (right), for B of 8, 12, and 16 from outside curve to inside. The probability densities plotted are 1, $10^{-1}, 10^{-2}, \ldots, 10^{-5}$ in the central and the single-scattering regions and 10^{-7}, 10^{-9} in the double-scattering region.

2.5 Molière simultaneous distribution with ionization

Integrating eq. (11) partly using *mathematica* [25], we have the analytical solution of simultaneous spectral density with ionization, as

$$\begin{aligned}\ln 2\pi\tilde{f} = \frac{\theta_{\rm M}^2 E_0 E}{4B(E_0-E)^2}\Bigg\{\eta t\Bigg[&(\zeta+\eta t)\ln\frac{\theta_{\rm M}^2(\zeta+\eta t)^2}{4e^B}\\ &-\zeta\ln\frac{\theta_{\rm M}^2\zeta^2}{4e^B}-\frac{E_0+E}{E_0-E}\eta t\ln\frac{E_0}{E}\Bigg]\\ &+(E\eta t-\varepsilon t\zeta)\Bigg[\frac{\zeta+\eta t}{E_0}\ln\frac{\theta_{\rm M}^2(\zeta+\eta t)^2}{4e^{B+2}}\\ &-\frac{\zeta}{E}\ln\frac{\theta_{\rm M}^2\zeta^2}{4e^{B+2}}-\left(\frac{\zeta+\eta t}{E_0}+\frac{\zeta}{E}\right)\ln\frac{E_0}{E}\Bigg]\\ &-\frac{(E\eta t-\varepsilon t\zeta)\eta t}{E_0-E}\Bigg[\ln\frac{E_0^2(\eta t)^2}{(E\eta t-\varepsilon t\zeta)^2}\ln\frac{\theta_{\rm M}^2(\zeta+\eta t)^2}{4e^B}\\ &-\ln\frac{E^2(\eta t)^2}{(E\eta t-\varepsilon t\zeta)^2}\ln\frac{\theta_{\rm M}^2\zeta^2}{4e^B}\\ &+4\,{\rm Li}_2\left(-\frac{(E_0-E)(\zeta+\eta t)}{E\eta t-\varepsilon t\zeta}\right)\\ &-4\,{\rm Li}_2\left(-\frac{(E_0-E)\zeta}{E\eta t-\varepsilon t\zeta}\right)\Bigg]\Bigg\},\end{aligned} \tag{25}$$

with B and $\theta_{\rm M}$ of eqs. (9) and (10), where ${\rm Li}_2(z)$ denotes the dilogarithm function indicated in appendix A[1]. The spectral density indicates that the simultaneous distribution between the deflection angle θ and the chord-angle $\psi \equiv y/t$, both scaled by $\theta_{\rm M}$, depends only on the expansion parameter B and the fractional energy E/E_0. The simultaneous distribution with fractional energy-loss, $(E_0 - E)/E_0$, of 1/4 and 1/2 are derived numerically through eq. (15)[2] as indicated in contour maps of the probability density in fig. 5, whose characteristic patterns appearing in the peripheral regions are discussed later in subsect. 3.3.

3 Relating problems and discussions

3.1 Molière simultaneous distribution expressed by power series with B^{-1}

The spectral density of the Molière simultaneous distribution under the fixed energy condition of eq. (24) can be expressed as

$$\begin{aligned}\tilde{f} = \frac{1}{2\pi}\exp\Bigg[&-\frac{\theta_{\rm M}^2}{4}\left(\zeta^2+\zeta\eta t+\frac{\eta^2t^2}{3}\right)+\frac{\theta_{\rm M}^2/B}{12\eta t}\\ &\times\left\{(\zeta+\eta t)^3\ln\frac{\theta_{\rm M}^2(\zeta+\eta t)^2}{4e^{2/3}}-\zeta^3\ln\frac{\theta_{\rm M}^2\zeta^2}{4e^{2/3}}\right\}\Bigg].\end{aligned} \tag{26}$$

We can expand the density by power series with B^{-1} as

$$\begin{aligned}\tilde{f} = \frac{1}{2\pi}e^{-\frac{\theta_{\rm M}^2}{4}(\zeta^2+\zeta\eta t+\frac{\eta^2t^2}{3})}\sum_{k=0}^{\infty}\frac{1}{k!}\frac{(\theta_{\rm M}^2/B)^k}{(12\eta t)^k}\\ \times\left\{(\zeta+\eta t)^3\ln\frac{\theta_{\rm M}^2(\zeta+\eta t)^2}{4e^{2/3}}-\zeta^3\ln\frac{\theta_{\rm M}^2\zeta^2}{4e^{2/3}}\right\}^k,\end{aligned} \tag{27}$$

so we find the Molière simultaneous distribution is expressed by power series with B^{-1} as

$$f(\theta,\psi,t) = f^{(0)}(\theta,\psi)+B^{-1}f^{(1)}(\theta,\psi)+B^{-2}f^{(2)}(\theta,\psi)+\ldots, \tag{28}$$

with the t-dependent B of eq. (9) and the B-independent series-coefficient functions of

$$\begin{aligned}f^{(k)}(\theta,\psi) = \frac{1/k!}{4\pi^2}\iint e^{-i\theta\zeta-i\psi\eta t}\left(\frac{\theta_{\rm M}^2}{12\eta t}\right)^k\\ \times\left\{(\zeta+\eta t)^3\ln\frac{\theta_{\rm M}^2(\zeta+\eta t)^2}{4e^{2/3}}-\zeta^3\ln\frac{\theta_{\rm M}^2\zeta^2}{4e^{2/3}}\right\}^k\\ \times e^{-\frac{\theta_{\rm M}^2}{4}(\zeta^2+\zeta\eta t+\frac{\eta^2t^2}{3})}\,{\rm d}\zeta\,{\rm d}(\eta t),\end{aligned} \tag{29}$$

similarly as the series expansion of the Molière angular distribution [2].

[1] Details of the dilogarithm function are indicated in, *e.g.*, `http://en.wikipedia.org/wiki/Spence's_function`.

[2] We evaluated the probability densities by numerical integration of eq. (15), though in the case of fractional energy-loss of 1/4, we evaluated the density through series expansion of $f^{(0)} + B^{-1}f^{(1)} + B^{-2}f^{(2)}$ indicated in subsect. 3.1, to reduce computation time.

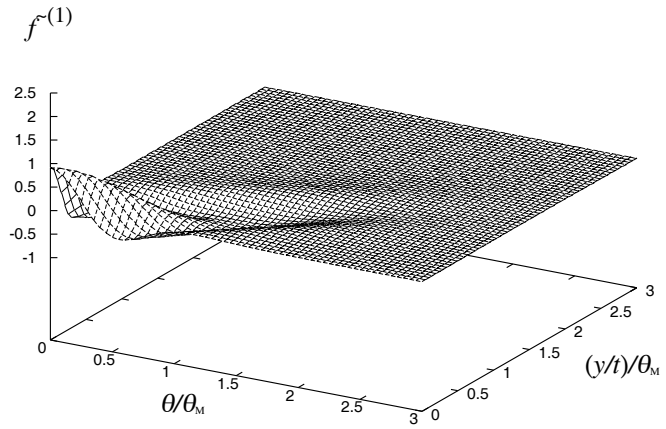

Fig. 6. Series-coefficient function of $f^{(1)}(\theta,\psi)$ with the variables θ and $\psi \equiv y/t$ scaled by $\theta_{\rm M}$.

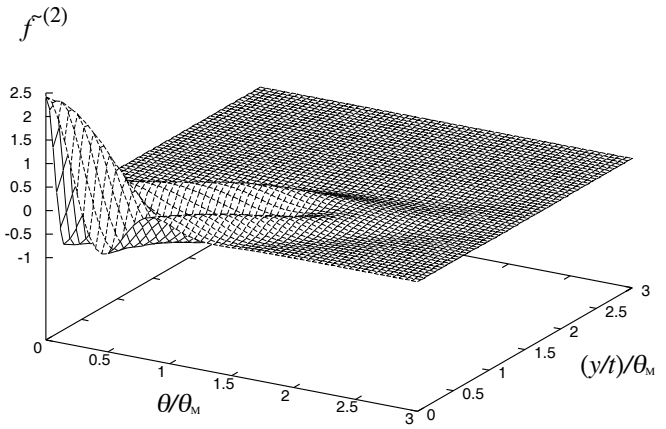

Fig. 7. Series-coefficient function of $f^{(2)}(\theta,\psi)$ with the variables θ and $\psi \equiv y/t$ scaled by $\theta_{\rm M}$.

Especially for the first three series-coefficient functions, we have

$$f^{(0)}(\theta,\psi) = \frac{1}{4\pi^2}\iint e^{-i\theta\zeta - i\psi\eta t} e^{-\frac{\theta_{\rm M}^2}{4}(\zeta^2+\zeta\eta t+\frac{\eta^2 t^2}{3})}\mathrm{d}\zeta\,\mathrm{d}(\eta t)$$

$$= \frac{2\sqrt{3}}{\pi\theta_{\rm M}^2}\exp\left[-\frac{4}{\theta_{\rm M}^2}\left(\theta^2 - 3\theta\psi + 3\psi^2\right)\right], \qquad (30)$$

$$f^{(1)}(\theta,\psi) = \frac{1}{4\pi^2}\iint e^{-i\theta\zeta - i\psi\eta t} e^{-\frac{\theta_{\rm M}^2}{4}(\zeta^2+\zeta\eta t+\frac{\eta^2 t^2}{3})}$$

$$\times\left\{\frac{\theta_{\rm M}^2}{4}\left(\zeta^2+\zeta\eta t+\frac{\eta^2 t^2}{3}\right)\ln\frac{\theta_{\rm M}^2\zeta^2}{4e^{2/3}}\right.$$

$$\left.+\frac{\theta_{\rm M}^2(\zeta+\eta t)^3}{12\eta t}\ln\left(1+\frac{\eta t}{\zeta}\right)^2\right\}\mathrm{d}\zeta\,\mathrm{d}(\eta t), \qquad (31)$$

$$f^{(2)}(\theta,\psi) = \frac{1/2!}{4\pi^2}\iint e^{-i\theta\zeta - i\psi\eta t} e^{-\frac{\theta_{\rm M}^2}{4}(\zeta^2+\zeta\eta t+\frac{\eta^2 t^2}{3})}$$

$$\times\left\{\frac{\theta_{\rm M}^2}{4}\left(\zeta^2+\zeta\eta t+\frac{\eta^2 t^2}{3}\right)\ln\frac{\theta_{\rm M}^2\zeta^2}{4e^{2/3}}\right.$$

$$\left.+\frac{\theta_{\rm M}^2(\zeta+\eta t)^3}{12\eta t}\ln\left(1+\frac{\eta t}{\zeta}\right)^2\right\}^2\mathrm{d}\zeta\,\mathrm{d}(\eta t), \qquad (32)$$

where at $|\frac{\eta t}{\zeta}| \le 0.01$ we evaluate

$$\frac{\theta_{\rm M}^2(\zeta+\eta t)^3}{12\eta t}\ln\left(1+\frac{\eta t}{\zeta}\right)^2 \simeq$$

$$\frac{\theta_{\rm M}^2(\zeta+\eta t)^3}{6\zeta}\left(1-\frac{\eta t}{2\zeta}+\frac{\eta^2 t^2}{3\zeta^2}-\dots\right). \qquad (33)$$

$f^{(0)}(\theta,\psi)$ derived analytically is a 2-dimensional Gaussian, already indicated in eq. (23). $f^{(1)}(\theta,\psi)$ and $f^{(2)}(\theta,\psi)$ are derived numerically as indicated in figs. 6 and 7 and given in tables 1 and 2 for representative radial directions in the θ-ψ coordinate. Then we can derive the simultaneous distributions accurately enough by the first three terms of the power series (28), easily with B from eq. (9), $f^{(0)}$ of eq. (30), and $f^{(1)}$, $f^{(2)}$ of tables 1 and 2 especially on the radial lines indicated in the tables without applying the numerical integration of eq. (15). The distributions derived by the first three terms of the power series agree very well with those derived by the numerical integration of eq. (15), as compared in fig. 8 on the radial lines of $\theta = 0$ and $\psi \equiv y/t = 0$ for $B = 8$.

Note that the term $f^{(k)}(\theta,\psi)$ for $k \ge 1$ does not contribute to the probability of simultaneous distribution with θ and ψ as a whole, as confirmed by

$$\int_{-\infty}^{\infty}\mathrm{d}\psi\int_{-\infty}^{\infty}\mathrm{d}\theta f^{(k)}(\theta,\psi) =$$

$$\lim_{\eta t\to 0}\left[\lim_{\zeta\to 0}\frac{1}{k!}\left(\frac{\theta_{\rm M}^2}{12\eta t}\right)^k\left\{(\zeta+\eta t)^3\ln\frac{(\zeta+\eta t)^2}{4e^{2/3}}\right.\right.$$

$$\left.\left.-\zeta^3\ln\frac{\zeta^2}{4e^{2/3}}\right\}^k e^{-\frac{\theta_{\rm M}^2}{4}(\zeta^2+\zeta\eta t+\frac{\eta^2 t^2}{3})}\right] = 0 \quad (\text{for } k \ge 1). \qquad (34)$$

3.2 A cross-section dividing model to interpret the series expansion of the Molière simultaneous distribution

We divide the screened single-scattering cross-section $\sigma(\chi)$ of eq. (2) as [4]

$$\sigma(\chi) = \sigma_{\rm M}(\chi) + \sigma_{\rm L}(\chi), \qquad (35)$$

where the moderate scattering $\sigma_{\rm M}(\chi)$ and the large-angle scattering $\sigma_{\rm L}(\chi)$ are divided at

$$\chi_{\rm B} = e^{B/2}\sqrt{e}\chi_a. \qquad (36)$$

Table 1. Series-coefficient function $f^{(1)}(\theta,\psi)$ on the radial lines with the azimuthal angle of φ, or $\theta=\rho\cos\varphi$ and $\psi=\rho\sin\varphi$. θ, ψ, and ρ are scaled by $\theta_{\rm M}$. $f^{(1)}(0,0)=9.106\text{e-}01$.

ρ	$\varphi=0$	$\varphi=\pi/6$	$\varphi=\pi/3$	$\varphi=\pi/2$	$\varphi=2\pi/3$	$\varphi=5\pi/6$
0.1	7.939e-01	8.888e-01	7.675e-01	5.735e-01	4.971e-01	5.969e-01
0.2	4.936e-01	8.251e-01	4.094e-01	−6.495e-02	−1.902e-01	−1.380e-02
0.3	1.314e-01	7.253e-01	3.185e-03	−4.105e-01	−4.167e-01	−3.733e-01
0.4	−1.644e-01	5.976e-01	−2.913e-01	−3.494e-01	−2.410e-01	−3.411e-01
0.5	−3.180e-01	4.527e-01	−4.027e-01	−1.525e-01	−5.398e-02	−1.509e-01
0.6	−3.267e-01	3.018e-01	−3.585e-01	−2.727e-02	1.153e-02	−1.595e-02
0.7	−2.405e-01	1.557e-01	−2.383e-01	9.890e-03	1.405e-02	2.741e-02
0.8	−1.238e-01	2.371e-02	−1.163e-01	1.006e-02	6.643e-03	2.564e-02
0.9	−2.428e-02	−8.689e-02	−3.139e-02	4.772e-03	2.487e-03	1.537e-02
1.0	3.805e-02	−1.717e-01	1.151e-02	1.742e-03	8.957e-04	8.123e-03
1.1	6.486e-02	−2.290e-01	2.493e-02	5.684e-04	3.306e-04	4.263e-03
1.2	6.783e-02	−2.598e-01	2.366e-02	1.777e-04	1.248e-04	2.310e-03
1.3	5.916e-02	−2.669e-01	1.775e-02	5.455e-05	4.741e-05	1.292e-03
1.4	4.723e-02	−2.547e-01	1.195e-02	1.643e-05	1.787e-05	7.383e-04
1.5	3.623e-02	−2.282e-01	7.676e-03	4.823e-06	6.628e-06	4.278e-04
1.6	2.751e-02	−1.927e-01	4.867e-03	1.370e-06	2.406e-06	2.499e-04
1.7	2.106e-02	−1.529e-01	3.106e-03	3.749e-07	8.519e-07	1.467e-04
1.8	1.638e-02	−1.129e-01	2.008e-03	9.846e-08	2.933e-07	8.619e-05
1.9	1.297e-02	−7.556e-02	1.316e-03	2.476e-08	9.803e-08	5.063e-05
2.0	1.044e-02	−4.300e-02	8.722e-04	5.950e-09	3.174e-08	2.968e-05
2.1	8.537e-03	−1.628e-02	5.827e-04	1.364e-09	9.944e-09	1.733e-05
2.2	7.067e-03	4.320e-03	3.914e-04	2.991e-10	3.011e-09	1.008e-05
2.3	5.913e-03	1.909e-02	2.638e-04	6.313e-11	8.802e-10	5.827e-06
2.4	4.994e-03	2.873e-02	1.781e-04	1.249e-11	2.482e-10	3.347e-06
2.5	4.253e-03	3.412e-02	1.204e-04	1.387e-12	6.747e-11	1.909e-06
2.6	3.648e-03	3.622e-02	8.138e-05	−8.856e-13	1.767e-11	1.080e-06
2.7	3.150e-03	3.594e-02	5.496e-05	−4.881e-13	4.468e-12	6.064e-07
2.8	2.736e-03	3.406e-02	3.706e-05	6.913e-13	1.083e-12	3.374e-07
2.9	2.390e-03	3.124e-02	2.494e-05	1.348e-12	2.363e-13	1.860e-07
3.0	2.098e-03	2.797e-02	1.675e-05	8.406e-13	4.347e-14	1.016e-07
3.1	1.850e-03	2.459e-02	1.121e-05	−4.193e-13	1.691e-14	5.491e-08
3.2	1.638e-03	2.134e-02	7.483e-06	−1.335e-12	1.161e-14	2.938e-08
3.3	1.456e-03	1.836e-02	4.976e-06	−1.086e-12	−4.968e-15	1.556e-08
3.4	1.299e-03	1.571e-02	3.297e-06	1.371e-13	−1.339e-14	8.149e-09
3.5	1.163e-03	1.341e-02	2.175e-06	1.265e-12	−2.151e-15	4.222e-09
3.6	1.045e-03	1.144e-02	1.429e-06	1.283e-12	6.124e-15	2.163e-09
3.7	9.415e-04	9.787e-03	9.348e-07	1.479e-13	−2.202e-15	1.095e-09
3.8	8.507e-04	8.398e-03	6.086e-07	−1.138e-12	−6.768e-15	5.484e-10
3.9	7.707e-04	7.239e-03	3.943e-07	−1.416e-12	1.128e-15	2.713e-10
4.0	7.000e-04	6.271e-03	2.542e-07	−4.224e-13	2.821e-15	1.327e-10
4.1	6.373e-04	5.463e-03	1.630e-07	9.572e-13	−5.541e-15	6.407e-11
4.2	5.816e-04	4.785e-03	1.040e-07	1.479e-12	−5.568e-15	3.057e-11
4.3	5.319e-04	4.214e-03	6.598e-08	6.748e-13	3.101e-15	1.441e-11
4.4	4.874e-04	3.730e-03	4.163e-08	−7.270e-13	3.480e-15	6.707e-12
4.5	4.475e-04	3.318e-03	2.612e-08	−1.467e-12	−1.873e-15	3.083e-12
4.6	4.117e-04	2.965e-03	1.629e-08	−8.966e-13	−5.534e-16	1.397e-12
4.7	3.794e-04	2.660e-03	1.010e-08	4.606e-13	5.103e-15	6.249e-13
4.8	3.502e-04	2.396e-03	6.229e-09	1.391e-12	4.151e-15	2.775e-13
4.9	3.238e-04	2.166e-03	3.817e-09	1.080e-12	−5.501e-16	1.242e-13
5.0	2.999e-04	1.964e-03	2.325e-09	−1.745e-13	−1.334e-15	5.624e-14
5.5	2.087e-04	1.254e-03	1.773e-10	1.290e-12	4.630e-15	4.060e-15
6.0	1.498e-04	8.451e-04	1.150e-11	5.131e-13	8.644e-15	−2.877e-15
6.5	1.104e-04	5.927e-04	6.321e-13	−1.129e-12	7.577e-16	−6.694e-15
7.0	8.319e-05	4.292e-04	2.883e-14	−8.049e-13	6.337e-16	−3.657e-16
7.5	6.388e-05	3.191e-04	1.093e-15	9.861e-13	5.755e-15	−1.047e-15
8.0	4.988e-05	2.424e-04	2.539e-16	1.243e-12	6.844e-16	−1.668e-15
8.5	3.952e-05	1.877e-04	−1.069e-15	−5.201e-13	−5.090e-15	−6.774e-16
9.0	3.172e-05	1.477e-04	−2.111e-17	−1.425e-12	−4.723e-16	1.923e-15
9.5	2.576e-05	1.179e-04	2.230e-15	−3.169e-14	2.644e-16	3.154e-15
10.0	2.114e-05	9.525e-05	−1.624e-15	1.289e-12	−8.001e-15	4.586e-15

Table 2. Series-coefficient function $f^{(2)}(\theta,\psi)$ on the radial lines with the azimuthal angle of φ, or $\theta=\rho\cos\varphi$ and $\psi=\rho\sin\varphi$. θ, ψ, and ρ are scaled by $\theta_{\rm M}$. $f^{(2)}(0,0)=2.416\text{e+}00$.

ρ	$\varphi=0$	$\varphi=\pi/6$	$\varphi=\pi/3$	$\varphi=\pi/2$	$\varphi=2\pi/3$	$\varphi=5\pi/6$
0.1	2.011e+00	2.342e+00	1.916e+00	1.263e+00	1.018e+00	1.344e+00
0.2	1.029e+00	2.128e+00	7.485e-01	−5.425e-01	−7.802e-01	−4.006e-01
0.3	2.826e-04	1.799e+00	−3.668e-01	−9.139e-01	−6.846e-01	−8.565e-01
0.4	−6.090e-01	1.392e+00	−8.853e-01	−2.680e-01	2.486e-02	−2.698e-01
0.5	−6.641e-01	9.489e-01	−7.635e-01	1.432e-01	1.605e-01	1.669e-01
0.6	−3.534e-01	5.150e-01	−3.361e-01	1.207e-01	3.423e-02	1.532e-01
0.7	1.914e-02	1.284e-01	3.313e-02	2.059e-02	−1.536e-02	2.249e-02
0.8	2.431e-01	−1.821e-01	1.855e-01	−8.391e-03	−7.683e-03	−3.020e-02
0.9	2.764e-01	−4.002e-01	1.626e-01	−1.765e-03	1.062e-03	−2.545e-02
1.0	1.910e-01	−5.225e-01	7.678e-02	4.417e-03	2.999e-03	−1.198e-02
1.1	8.007e-02	−5.570e-01	7.186e-03	5.163e-03	2.520e-03	−4.468e-03
1.2	1.200e-04	−5.205e-01	−2.389e-02	3.882e-03	1.766e-03	−1.454e-03
1.3	−3.652e-02	−4.343e-01	−2.732e-02	2.544e-03	1.182e-03	−3.028e-04
1.4	−4.219e-02	−3.212e-01	−1.973e-02	1.597e-03	7.808e-04	1.664e-04
1.5	−3.376e-02	−2.017e-01	−1.132e-02	9.982e-04	5.149e-04	3.576e-04
1.6	−2.263e-02	−9.193e-02	−5.495e-03	6.326e-04	3.413e-04	4.181e-04
1.7	−1.373e-02	−2.785e-03	−2.223e-03	4.102e-04	2.287e-04	4.137e-04
1.8	−7.945e-03	6.051e-02	−5.844e-04	2.733e-04	1.555e-04	3.781e-04
1.9	−4.568e-03	9.748e-02	1.888e-04	1.871e-04	1.077e-04	3.300e-04
2.0	−2.701e-03	1.112e-01	5.387e-04	1.313e-04	7.599e-05	2.795e-04
2.1	−1.676e-03	1.069e-01	6.833e-04	9.432e-05	5.468e-05	2.318e-04
2.2	−1.100e-03	9.057e-02	7.243e-04	6.910e-05	4.007e-05	1.894e-04
2.3	−7.613e-04	6.792e-02	7.105e-04	5.152e-05	2.986e-05	1.532e-04
2.4	−5.526e-04	4.372e-02	6.676e-04	3.901e-05	2.260e-05	1.229e-04
2.5	−4.176e-04	2.142e-02	6.101e-04	2.994e-05	1.734e-05	9.814e-05
2.6	−3.265e-04	3.089e-03	5.467e-04	2.326e-05	1.347e-05	7.818e-05
2.7	−2.628e-04	−1.036e-02	4.829e-04	1.827e-05	1.059e-05	6.223e-05
2.8	−2.166e-04	−1.896e-02	4.217e-04	1.450e-05	8.401e-06	4.958e-05
2.9	−1.823e-04	−2.331e-02	3.651e-04	1.161e-05	6.728e-06	3.960e-05
3.0	−1.560e-04	−2.433e-02	3.139e-04	9.373e-06	5.434e-06	3.175e-05
3.1	−1.353e-04	−2.301e-02	2.685e-04	7.628e-06	4.424e-06	2.556e-05
3.2	−1.187e-04	−2.026e-02	2.286e-04	6.252e-06	3.627e-06	2.069e-05
3.3	−1.052e-04	−1.683e-02	1.941e-04	5.159e-06	2.993e-06	1.685e-05
3.4	−9.386e-05	−1.327e-02	1.644e-04	4.283e-06	2.486e-06	1.380e-05
3.5	−8.432e-05	−9.936e-03	1.391e-04	3.577e-06	2.077e-06	1.137e-05
3.6	−7.616e-05	−7.037e-03	1.176e-04	3.004e-06	1.744e-06	9.430e-06
3.7	−6.909e-05	−4.653e-03	9.946e-05	2.535e-06	1.472e-06	7.866e-06
3.8	−6.293e-05	−2.785e-03	8.416e-05	2.150e-06	1.249e-06	6.599e-06
3.9	−5.750e-05	−1.385e-03	7.130e-05	1.832e-06	1.064e-06	5.567e-06
4.0	−5.269e-05	−3.794e-04	6.051e-05	1.567e-06	9.107e-07	4.721e-06
4.1	−4.840e-05	3.086e-04	5.146e-05	1.346e-06	7.825e-07	4.023e-06
4.2	−4.456e-05	7.533e-04	4.387e-05	1.161e-06	6.749e-07	3.444e-06
4.3	−4.111e-05	1.018e-03	3.751e-05	1.005e-06	5.842e-07	2.962e-06
4.4	−3.799e-05	1.156e-03	3.216e-05	8.727e-07	5.075e-07	2.557e-06
4.5	−3.517e-05	1.206e-03	2.767e-05	7.605e-07	4.423e-07	2.216e-06
4.6	−3.260e-05	1.199e-03	2.388e-05	6.648e-07	3.867e-07	1.928e-06
4.7	−3.027e-05	1.157e-03	2.067e-05	5.829e-07	3.391e-07	1.683e-06
4.8	−2.814e-05	1.094e-03	1.796e-05	5.126e-07	2.982e-07	1.474e-06
4.9	−2.619e-05	1.020e-03	1.565e-05	4.519e-07	2.630e-07	1.294e-06
5.0	−2.440e-05	9.430e-04	1.369e-05	3.995e-07	2.325e-07	1.140e-06
5.5	−1.740e-05	6.004e-04	7.322e-06	2.236e-07	1.302e-07	6.294e-07
6.0	−1.269e-05	3.775e-04	4.181e-06	1.318e-07	7.679e-08	3.673e-07
6.5	−9.432e-06	2.428e-04	2.515e-06	8.116e-08	4.728e-08	2.244e-07
7.0	−7.127e-06	1.606e-04	1.579e-06	5.183e-08	3.020e-08	1.425e-07
7.5	−5.466e-06	1.092e-04	1.027e-06	3.415e-08	1.990e-08	9.345e-08
8.0	−4.248e-06	7.602e-05	6.880e-07	2.313e-08	1.348e-08	6.305e-08
8.5	−3.342e-06	5.412e-05	4.732e-07	1.604e-08	9.351e-09	4.360e-08
9.0	−2.658e-06	3.928e-05	3.329e-07	1.136e-08	6.625e-09	3.081e-08
9.5	−2.135e-06	2.901e-05	2.389e-07	8.201e-09	4.783e-09	2.220e-08
10.0	−1.731e-06	2.176e-05	1.746e-07	6.020e-09	3.512e-09	1.627e-08

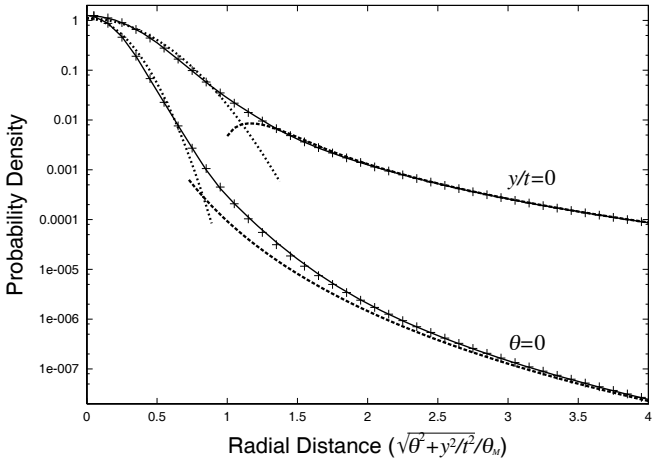

Fig. 8. Comparison of the probability densities of the simultaneous distribution for $B = 8$ under the fixed energy condition, between those expressed by the series expansion of $f^{(0)} + B^{-1}f^{(1)} + B^{-2}f^{(2)}$ (solid lines) and those derived by the numerical inverse transforms of eq. (15) (+ dots), on the radial lines of $y/t = 0$ and $\theta = 0$ with the radial distance scaled by $\theta_{\rm M}$. The first series-expansion terms of $f^{(0)}(\theta, y/t)$ in the central region (dot lines), as well as $B^{-1}f^{(1)}(\theta, 0)$ and $f_2(0, y/t, t)$ in the peripheral region (broken lines), are also indicated.

As we have [4,13]

$$2\pi\int_0^\infty \{J_0(\zeta'\chi)-1\}\,\sigma_{\rm M}(\chi)\chi\,{\rm d}\chi = -\frac{B}{\Omega}\frac{K^2\zeta'^2}{4E^2} + \mathcal{O}(\zeta'^4),$$
$$2\pi\int_0^\infty \{J_0(\zeta'\chi)-1\}\,\sigma_{\rm L}(\chi)\chi\,{\rm d}\chi = \frac{1}{\Omega}\frac{K^2\zeta'^2}{4E^2}\ln\frac{e^B K^2\zeta'^2}{e^\Omega 4E^2} + \mathcal{O}(\zeta'^4), \quad (37)$$

the diffusion equation (6) is described as

$$\frac{\partial\tilde{F}}{\partial t'} = \vec{\eta}\frac{\partial\tilde{F}}{\partial\vec{\zeta}'} + 2\pi\tilde{F}\int_0^\infty \{J_0(\zeta'\chi)-1\} \times\{\sigma_{\rm M}(\chi)+\sigma_{\rm L}(\chi)\}\,\chi\,{\rm d}\chi$$
$$= \vec{\eta}\frac{\partial\tilde{F}}{\partial\vec{\zeta}'} - \frac{B}{\Omega}\frac{K^2\zeta'^2}{4E^2}\tilde{F} + \frac{1}{\Omega}\frac{K^2\zeta'^2}{4E^2}\tilde{F}\ln\frac{e^B K^2\zeta'^2}{e^\Omega 4E^2}. \quad (38)$$

The differential term with $\vec{\zeta}'$ vanishes when we replace the variable $\vec{\zeta}'$ by eq. (7), then we have

$$\ln 4\pi^2\tilde{F} = -\frac{B}{\Omega}\int_0^t \frac{K^2(\vec{\zeta}+(t-t')\vec{\eta})^2}{4E^2}\,{\rm d}t' + \frac{1}{\Omega}\int_0^t \frac{K^2(\vec{\zeta}+(t-t')\vec{\eta})^2}{4E^2} \times\ln\frac{e^B K^2(\vec{\zeta}+(t-t')\vec{\eta})^2}{e^\Omega 4E^2}\,{\rm d}t', \quad (39)$$

under the fixed energy condition, so that we have the spectral density for the projected components

$$\ln 2\pi\tilde{f} = -\int_0^1 \frac{\theta_{\rm M}^2(\zeta+\eta tu)^2}{4}\,{\rm d}u + \frac{1}{B}\int_0^1 \frac{\theta_{\rm M}^2(\zeta+\eta tu)^2}{4} \times\ln\frac{\theta_{\rm M}^2(\zeta+\eta tu)^2}{4}\,{\rm d}u$$
$$= -\frac{\theta_{\rm M}^2}{4}\left(\zeta^2+\zeta\eta t+\frac{\eta^2t^2}{3}\right) + \frac{\theta_{\rm M}^2/B}{12\eta t} \times\left\{(\zeta+\eta t)^3\ln\frac{\theta_{\rm M}^2(\zeta+\eta t)^2}{4e^{2/3}} - \zeta^3\ln\frac{\theta_{\rm M}^2\zeta^2}{4e^{2/3}}\right\}, \quad (40)$$

identical with eq. (24). It should be reminded that the former and the latter terms are the correction terms on the simultaneous distribution by the moderate scattering $\sigma_{\rm M}(\chi)$ and the large-angle scattering $\sigma_{\rm L}(\chi)$ expressed in the Fourier component, respectively. So the successive terms in the power series (27) with B^{-1} mean the Gaussian distribution of eq. (23) produced by $\sigma_{\rm M}(\chi)$ $(k = 0)$ and its corrected distributions by k-times scatterings of $\sigma_{\rm L}(\chi)$ within the thickness t $(k \geq 1)$, expressed in the Fourier component. The successive terms in the power series (28) for the simultaneous distribution have the same meaning.

The probability p of receiving $\sigma_{\rm L}(\chi)$ within the thickness t is evaluated as [4]

$$p \equiv \int_0^t {\rm d}t\int_0^\infty \sigma_{\rm L}(\chi)2\pi\chi\,{\rm d}\chi = \frac{t}{\pi\Omega}\frac{K^2}{E^2}\int_{\chi_{\rm B}}^\infty \chi^{-4}2\pi\chi\,{\rm d}\chi = e^{2C-2}/B, \quad (41)$$

so that we find the power series (28) with B^{-1} means the power series with the probability of receiving the low-frequent large-angle scattering $\sigma_{\rm L}(\chi)$ within the thickness t, which explains very rapid convergence of the power series (28) for the Molière simultaneous distribution as the traditional power series for the Molière angular distribution [4].

3.3 Contour patterns of probability density for the Molière simultaneous distribution

Contour maps of the probability density $f(\theta, \psi, t)$ for the simultaneous distribution with ionization are indicated in fig. 5 with θ and $\psi \equiv y/t$ scaled by $\theta_{\rm M}$. Those show B-independent elliptic patterns of 2-dimensional Gaussian at the central region of distribution $(\theta^2 + \psi^2 \ll \theta_{\rm M}^2)$, which are well approximated by the Gaussians of eq. (21), revealing as the limiting distribution at $B \to \infty$ (or $t \to \infty$ as indicated in fig. 1). The azimuthal angle λ for the major axis of the Gaussian in the θ-ψ coordinate is determined by the rotation angle introduced in subsect. 2.2 to remove $\theta'\psi'$

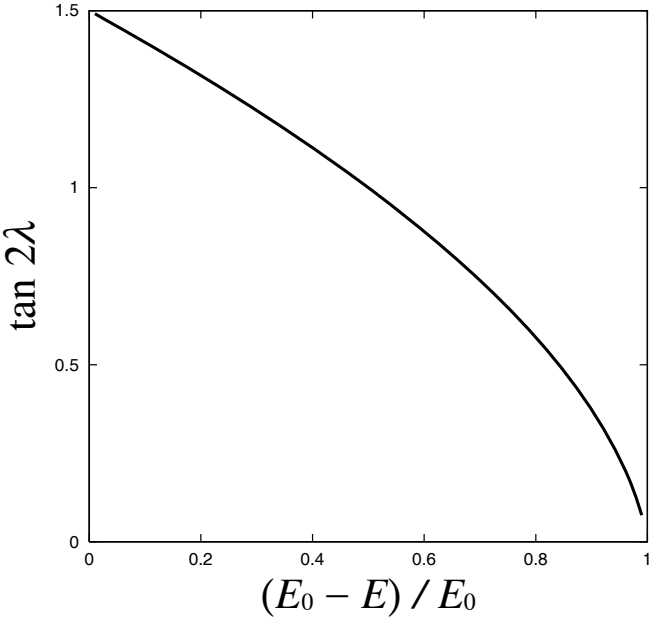

Fig. 9. Decrease of the azimuthal angle λ of the major axis for the central Gaussian distribution, with the dissipation of fractional energy.

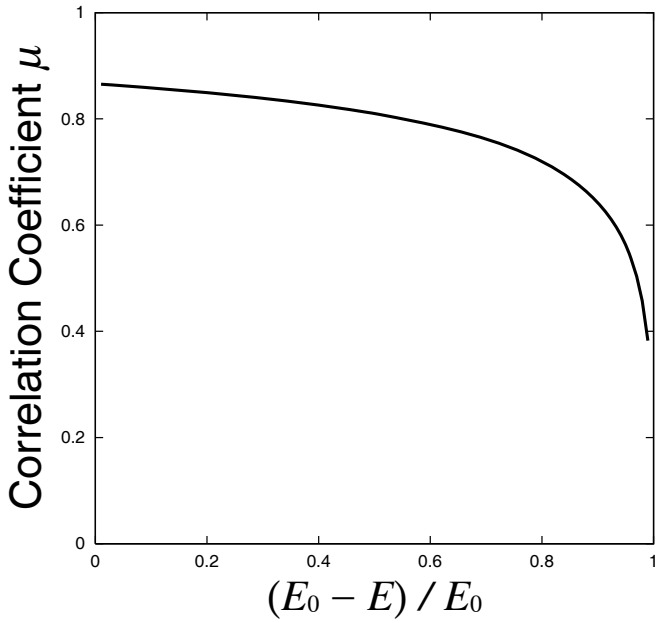

Fig. 10. Decrease of the correlation coefficient μ, with the dissipation of fractional energy.

term from eq. (21) in the θ'-ψ' coordinate. Thus we have

$$\tan 2\lambda = 2\left(\frac{E_0-E}{E_0}-\ln\frac{E_0}{E}\right)\Big/ \left(\frac{E_0+E}{E_0}-\frac{(E_0-E)^2}{E_0E}-\frac{2E}{E_0-E}\ln\frac{E_0}{E}\right), \tag{42}$$

which decreases from 3/2 to 0 with the increase of fractional energy-loss, $(E_0-E)/E_0$, as indicated in fig. 9. The correlation coefficient μ is expressed as [26]

$$\mu \equiv \frac{\langle\theta\cdot y/t\rangle_{\rm av}}{\sqrt{\langle\theta^2\rangle_{\rm av}\langle y^2/t^2\rangle_{\rm av}}} = \left(\ln\frac{E_0}{E}-1+\frac{E}{E_0}\right)\Big/ \sqrt{\left(\frac{E_0}{E}-\frac{E}{E_0}-2\ln\frac{E_0}{E}\right)\left(1-\frac{E}{E_0}\right)}, \tag{43}$$

which decreases from $\sqrt{3}/2$ to 0 with the increase of fractional energy-loss, as indicated in fig. 10.

The probability density in the peripheral region of $\theta^2+\psi^2 \gg \theta_{\rm M}^2$ with $\psi(\psi-\theta)<0$ (single-scattering region) depends only on θ and does not depend on y/t under the fixed energy condition. We interpret the simultaneous distribution in this region by the single scattering illustrated in fig. 11, taking account of ionization loss. Probability $\sigma_{\rm p}(\theta_y)\,{\rm d}\theta_y\,{\rm d}t'$ for charged particles to be scattered in the projected angle between θ_y and $\theta_y+{\rm d}\theta_y$ within the thickness of ${\rm d}t'$ is derived from the spatial angular distribution

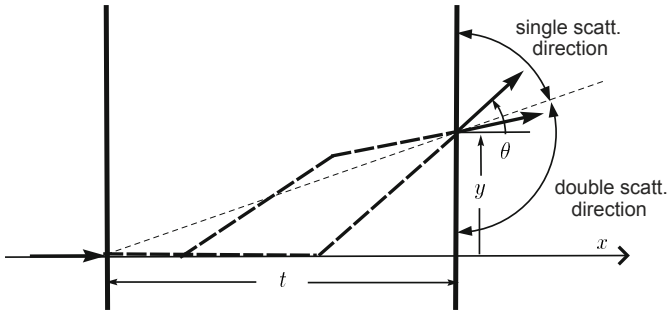

Fig. 11. The single- and the double-scattering dominant directions in the peripheral regions.

expressed in eq. (2), as

$$\sigma_{\rm p}(\theta_y)\,{\rm d}\theta_y\,{\rm d}t' = \frac{1}{\pi\Omega}\frac{K^2}{E'^2}\,{\rm d}\theta_y\,{\rm d}t'\int_{-\infty}^{\infty}\frac{{\rm d}\theta_z}{(\theta_y^2+\theta_z^2)^2} = \frac{1}{2\Omega}\frac{K^2}{E'^2}\theta_y^{-3}\,{\rm d}\theta_y\,{\rm d}t', \tag{44}$$

where the energy decreases as $E'=E_0-\varepsilon t'$ according to eq. (4). So the probability of simultaneous distribution determined by the single scattering, $f_1(\theta,\psi,t)\,{\rm d}\theta\,{\rm d}\psi$, is evaluated as

$$f_1(\theta,\psi,t)\,{\rm d}\theta\,{\rm d}\psi = \frac{K^2}{2\Omega}\,{\rm d}\theta\,{\rm d}y\int_0^t\frac{\theta^{-3}}{E^2}\delta(y-(t-t')\theta)\,{\rm d}t' = \frac{1}{2\Omega}\frac{K^2\theta^{-4}}{(E+\varepsilon y/\theta)^2}\,{\rm d}\theta\,{\rm d}y = \frac{\theta_{\rm M}^2}{2B}\frac{E_0E}{(E+\varepsilon y/\theta)^2}\theta^{-4}\,{\rm d}\theta\,{\rm d}\frac{y}{t}, \tag{45}$$

where δ denotes the delta function. On the contrary in the peripheral region of $\theta^2+\psi^2\gg\theta_{\rm M}^2$ with $\psi(\psi-\theta)>0$

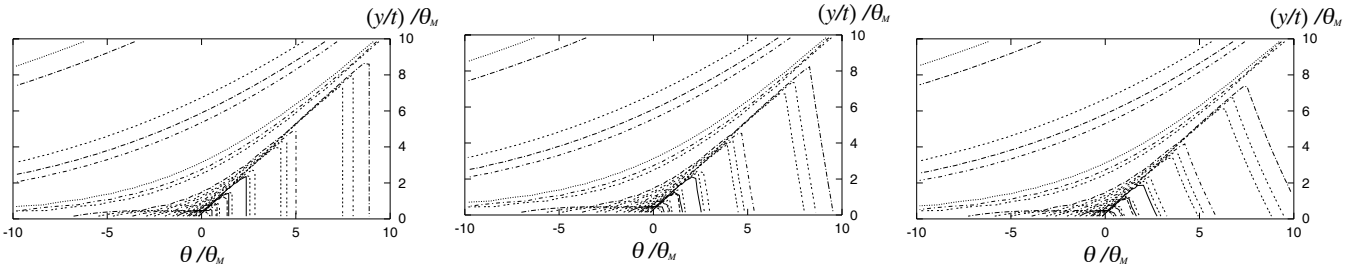

Fig. 12. Contour maps of the probability density of simultaneous distribution between the deflection angle θ and the chord-angle $\psi \equiv y/t$ with the both projected angles scaled by $\theta_{\rm M}$, predicted by the single and the double scatterings in cases of fixed energy (left), as well as with fractional energy loss of 1/4 (middle) and 1/2 (right), for B of 8, 12, and 16 from outside curve to inside. The probability densities plotted are 1, $10^{-1}, 10^{-2}, \ldots, 10^{-5}$ in the central and the single-scattering regions and 10^{-7}, 10^{-9}, 10^{-11} in the double-scattering region.

(double-scattering region), we can interpret the simultaneous distribution by the double scattering as illustrated in fig. 11. The probability of simultaneous distribution determined by the double scattering, $f_2(\theta,\psi,t)\,\mathrm{d}\theta\,\mathrm{d}\psi$, is evaluated as

$$\begin{aligned} f_2(\theta,\psi,t)\,\mathrm{d}\theta\,\mathrm{d}\psi &= \left(\frac{K^2}{2\Omega}\right)^2 \mathrm{d}\theta\,\mathrm{d}y \int_0^t \mathrm{d}t' \int_{y/(t-t')}^{\infty} \mathrm{d}\theta' \\ &\quad \times \frac{\theta'^{-3}}{E'^2} \int_{t'}^{t} \mathrm{d}t'' \frac{(\theta-\theta')^{-3}}{E''^2} \delta(y-(t-t')\theta' \\ &\quad -(t-t'')(\theta-\theta')) \\ &= \left(\frac{K^2}{2\Omega}\right)^2 \mathrm{d}\theta\,\mathrm{d}y \int_0^t \mathrm{d}t' \int_{y/(t-t')}^{\infty} \frac{\theta'^{-3}}{E'^2} \\ &\quad \times \frac{(\theta-\theta')^{-4}}{(E+\varepsilon(y-(t-t')\theta')/(\theta-\theta'))^2}\,\mathrm{d}\theta' \\ &= \left(\frac{\theta_{\rm M}^2}{2B}\right)^2 \mathrm{d}\theta\,\mathrm{d}\frac{y}{t} \int_0^t \frac{\mathrm{d}t'}{t} \frac{E_0 E}{E'^2} \int_{y/(t-t')}^{\infty} \\ &\quad \times \frac{E_0 E \theta'^{-3}(\theta-\theta')^{-2}}{(E_0 y/t + E(\theta-y/t) - E'\theta')^2}\,\mathrm{d}\theta'. \end{aligned} \tag{46}$$

The contour maps derived from $f_1(\theta,\psi,t)$ and $f_2(\theta,\psi,t)$ in case of fixed energy, as well as in cases with fractional energy loss, $(E_0-E)/E_0$, of 1/4 and 1/2 are indicated in fig. 12, which well explain the Molière simultaneous distributions of fig. 5 in the peripheral regions.

The contour lines of $f_1(\theta,\psi,t)$ run parallel to the (y/t)-axis in fig. 12 under the fixed energy condition ($\varepsilon = 0$), as the probability density of the single scattering depends only on θ and does not depend on the thickness t' or the lateral displacement $y \equiv (t-t')\theta$ in the evaluation of eq. (45). We derive the equation of the contour line of $f_1(\theta,\psi,t)$, which meets the θ-axis at θ_0. As it satisfies $f_1(\theta,\psi,t) = f_1(\theta_0,0,t)$, we have the equation

$$(E_0-E)\psi = E(\theta_0^2/\theta - \theta), \quad \text{for} \quad \psi(\psi-\theta) \le 0 \tag{47}$$

of hyperbola, which explains the parallel lines to (y/t)-axis under the fixed energy condition and the inclined lines under the process with ionization, appearing in the single-scattering region of the contour map in fig. 5.

The probability densities $f(\theta,\psi,t)$ on the radial lines of $\theta = 0$ and $y/t = 0$ under the fixed energy condition are indicated in fig. 8 for $B = 8$. Those in the central region are well explained by the Gaussian distributions of $f^{(0)}(\theta,\psi)$ as good first approximations, though substantial contributions from $B^{-1}f^{(1)}(\theta,\psi)$ and $B^{-2}f^{(2)}(\theta,\psi)$, or the first and the second correction terms on the Gaussian distributions by receiving the large-angle scattering $\sigma_{\rm L}(\chi)$ defined in subsect. 3.2, should be taken into account as pointed out by Scott [13]. The density in the peripheral region indicated on the radial line of $\theta = 0$ is well explained by $f_2(0,\psi,t) = (\theta_{\rm M}^4/168)B^{-2}\psi^{-6}$ derived by the double scattering. On the other hand, the density in the peripheral region on the radial line of $y/t = 0$ cannot be explained by $f_1(\theta,0,t)$ derived by the single scattering, as the density $f(\theta,0,t)$ in the peripheral region indicated in fig. 5 shows a little smaller value than $f_1(\theta,0,t)$ indicated in fig. 12. This density is well explained by $B^{-1}f^{(1)}(\theta,0)$ term, or the first correction term on the Gaussian distribution by receiving the above scattering $\sigma_{\rm L}(\chi)$, as indicated in fig. 8 [27].

3.4 Comparison of the Molière simultaneous distribution with an exact distribution based on a screened single-scattering model and limits of the Molière theory

It is well known that Molière's Fourier spectral density for his angular distribution [2] showed Gaussian at the central region of spectrum ($\theta_{\rm M}^2\zeta^2 + \theta_{\rm M}^2\eta^2t^2 \ll 1$), agreeing very well with an exact spectral density [9,10] derived under a model of screened single scattering [11,12]. Though with the increase of frequency, it began to depart from the exact spectral density and to increase and diverge after taking a deep minimum, so that the resultant Molière angular distribution wiggled especially in case of small B [9,10]. The Molière simultaneous spectral density of eq. (24) has also the same problem, as indicated in fig. 13 for $B = 8$. It has the peak value of $1/(2\pi)$ at $\zeta = \eta t = 0$ and decreases with 2-dimensional Gaussian at low-frequency regions of ζ and ηt. Though, it begins to increase after revealing a deep ditch and diverges at $\theta_{\rm M}^2\zeta^2 + \theta_{\rm M}^2\eta^2t^2 \gg 1$, which fact disturbs convergence of the numerical integration of

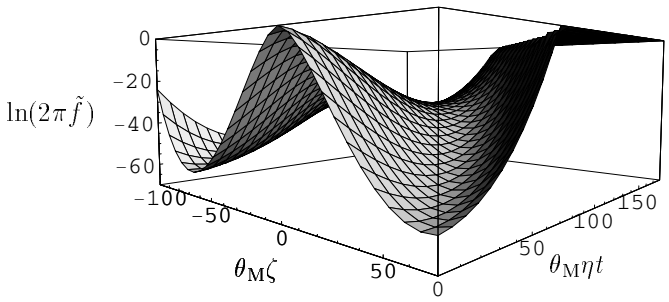

Fig. 13. Fourier spectral density (logarithmic value) of the Molière simultaneous distribution, for $B = 8$ under the fixed energy condition.

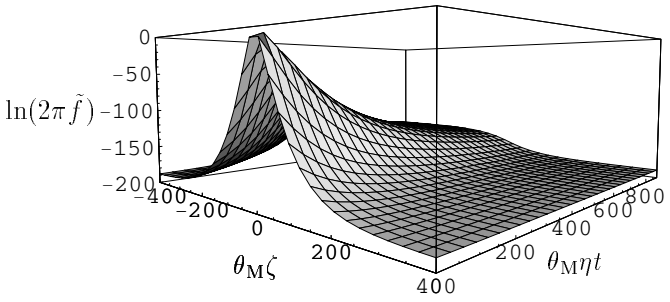

Fig. 14. Fourier spectral density (logarithmic value) of an exact simultaneous distribution, for $B = 8$ under the fixed energy condition.

eq. (15) to obtain the Molière simultaneous distribution in case of small B.

These problems vanished in derivation of the angular distribution by applying an exact spectral density derived under the well-known model of screened single scattering [11,12],

$$\sigma(\chi)2\pi\chi\,\mathrm{d}\chi\,\mathrm{d}t = \frac{1}{\pi\Omega}\frac{K^2}{E^2}\frac{1}{(\chi^2+\chi_a^2)^2}2\pi\chi\,\mathrm{d}\chi\,\mathrm{d}t. \quad (48)$$

We obtain the simultaneous distribution, based on this model. The diffusion equation for the Fourier spectral density is exactly described as

$$\frac{\partial\tilde{F}}{\partial t'} = \vec{\eta}\frac{\partial\tilde{F}}{\partial\vec{\zeta'}} + \frac{K^2/E^2}{\Omega\chi_a^2}\tilde{F}\left\{\chi_a\zeta' K_1(\chi_a\zeta') - 1\right\}, \quad (49)$$

instead of eq. (6) under the Molière theory where terms of $\mathcal{O}(\zeta'^4)$ were neglected [9,12,13]. K_1 denotes the modified Bessel function of the first order [28]. The differential term with $\vec{\zeta'}$ vanishes when we replace the variable $\vec{\zeta'}$ by eq. (7), thus we get the simultaneous spectral density for the projected components as

$$\begin{aligned}\tilde{f}(\zeta,\eta t,t) &= \frac{1}{2\pi}\exp\left[\frac{K^2t/E^2}{\Omega\chi_a^2}\int_0^1 \right.\\ &\quad\left.\times\left\{\chi_a|\zeta+\eta tu|K_1(\chi_a|\zeta+\eta tu|)-1\right\}\mathrm{d}u\right]\\ &= \frac{1}{2\pi}\exp\left[\frac{e^{B-1+2C}}{B}\left\{\int_0^1\frac{\theta_{\rm M}|\zeta+\eta tu|}{e^{(B-1+2C)/2}}\right.\right.\\ &\quad\left.\left.\times\ K_1\left(\frac{\theta_{\rm M}|\zeta+\eta tu|}{e^{(B-1+2C)/2}}\right)\mathrm{d}u-1\right\}\right], \end{aligned} \quad (50)$$

under the fixed energy condition, instead of eq. (24) derived by the Molière theory, with χ_a of eq. (3) expressed as

$$\chi_a = \theta_{\rm M}/e^{(B-1+2C)/2}, \quad (51)$$

according to eqs. (9) and (10).

The resultant spectral density is indicated in fig. 14 for $B = 8$, for wider regions of ζ and ηt than fig. 13. It also has the peak value of $1/(2\pi)$ at $\zeta = \eta t = 0$ and shows the same Gaussian decrease at low-frequency regions of ζ and ηt as the Molière spectral density of fig. 13. Though, it continues to decrease monotonously with the increase of $\zeta^2+\eta^2t^2$ and approaches to the finite limiting density of

$$\lim_{\zeta^2+\eta^2t^2\to\infty}\tilde{f}(\zeta,\eta t,t) = e^{-t/t_0}/(2\pi), \quad (52)$$

with

$$1/t_0 = K^2/(E^2\Omega\chi_a^2) = \Omega^{-1}e^{\Omega-1+2C}, \quad (53)$$

corresponding to the survival probability of the incident particle against the scattering of eq. (48) with the mean free path of t_0 [10]. Hence, the inverse Fourier transforms of eq. (12), applied to the spectral density of eq. (50) with the limiting density of $e^{-t/t_0}/(2\pi)$ subtracted, converges at any thickness of t and gives the exact simultaneous distribution between θ and y/t, removing the delta function corresponding to the survival probability of the incident charged particle, as in the derivation of exact angular distribution [10]. The exact simultaneous distribution expressed with the variables scaled by $\theta_{\rm M}$ depends only on the parameter B, under the fixed energy condition.

As the diffusion equation (6) under the Molière theory is a highly accurate approximation of the exact equation (49) for small $|\zeta'|$ [12], the resultant simple spectral density of eq. (24) agrees very well with the exact one of eq. (50) in the central region of spectrum, within the ditch observed in fig. 13. We compare the both in the contour map of fig. 15 for $B = 8$. We cannot find any visible difference between the both in the central region of spectrum where the numerical inverse transforms of eq. (15) converge. Thus the both simultaneous distributions derived by the respective spectral densities agree very well, as indicated in the contour map of fig. 16 for $B = 8$.

In case of small thicknesses of t (or the corresponding B determined by eq. (9)), the ditch is shallow reflecting the even high limiting density $e^{-t/t_0}/(2\pi)$ of the exact spectrum, so that the numerical integration of eq. (15) does not converge due to the divergence of spectral densities outside the ditch. With the increase of t, the ditch becomes deep reflecting the decrease of the limiting spectral density, so that the numerical integration begins to converge in the central region of spectrum. And in case of large enough t, we get the reliable Molière simultaneous distributions by the numerical inverse transforms of eq. (15) with the integration converged in the accurate

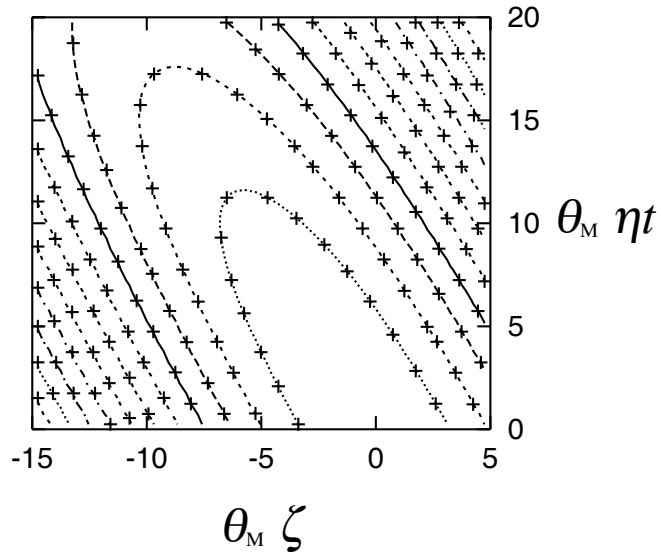

Fig. 15. The Fourier spectral densities, $2\pi\tilde{f}(\zeta, \eta t, t)$, are compared between the Molière's (line) and the exact one (+ dot) on the contour map for $B = 8$. The spectral densities plotted are $10^{-1}, 10^{-2}, \ldots, 10^{-11}$, from inside to outside.

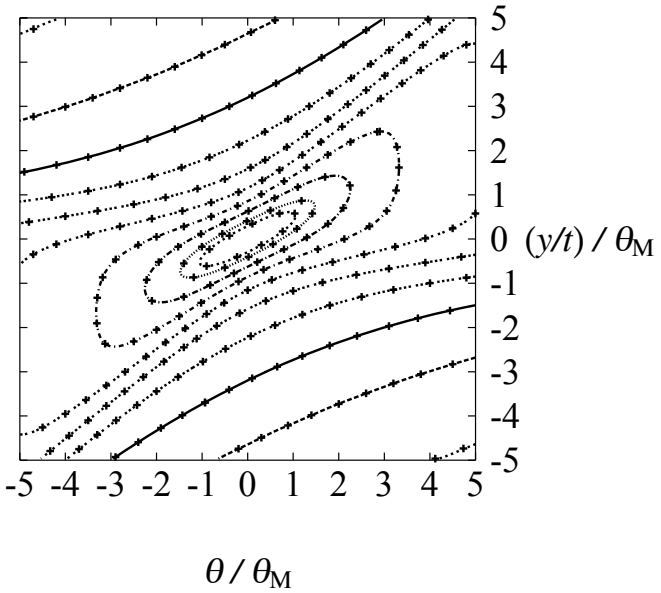

Fig. 16. The simultaneous distributions $f(\theta, y/t, t)$ are compared between the Molière's (line) and the exact one (+ dot) on the contour map for $B = 8$, with the both variables scaled by θ_M. The probability densities plotted are 1, $10^{-1}, \ldots, 10^{-9}$, from inside to outside.

region of spectrum, even under the process with ionization by applying the spectral density of eq. (25). On the other hand, we can get the exact simultaneous distributions under the fixed energy condition at any thickness of t (or the corresponding B) by applying the numerical integration of eq. (15) on the exact spectral density of eq. (50) with the limiting density of $e^{-t/t_0}/(2\pi)$ subtracted, though the spectral density expressed in a definite integral is rather complicated.

4 Conclusions

Simultaneous distribution between the deflection angle θ and the lateral displacement y for charged particles traversing through matter is derived under the Molière theory of multiple scattering with ionization. The distribution is evaluated by applying the numerical inverse Fourier transforms on the analytical Fourier spectral density solved by the differentially formulated Molière theory. The distributions are indicated on the contour maps of the probability density, which is characterized by three regions: the central region, the single-scattering region, and the double-scattering region, reflecting the properties of the multiple scattering, the single scattering, and the double scattering, respectively (sect. 2 and subsect. 3.3).

The simultaneous distribution with the both projected angles, θ and $\psi \equiv y/t$, scaled by θ_M is expressed in power series with B^{-1} under the fixed energy condition. The first three terms of the series, $f(\theta, \psi, t) = f^{(0)}(\theta, \psi) + B^{-1}f^{(1)}(\theta, \psi) + B^{-2}f^{(2)}(\theta, \psi)$, with B-independent series-coefficient functions, $f^{(0)}$ of eq. (30) and $f^{(1)}$, $f^{(2)}$ of the predetermined tables 1 and 2 for required radial directions in the θ-ψ coordinate, are effective in easy derivations of the probability density without applying the numerical integration of eq. (15) at required thicknesses of t, with the corresponding B and θ_M determined by eqs. (9) and (10) (subsect. 3.1).

The Molière simultaneous distribution expressed by the power series (28) with B^{-1} is well interpreted by the cross-section dividing model, as series of the central Gaussian distributions corrected successively by the k-times large-angle scatterings of $\sigma_L(\chi)$ within the thickness t. B^{-1} is proportional to the probability of receiving the scattering $\sigma_L(\chi)$ within the thickness t, so that we find the power series (28) shows very rapid convergence (subsect. 3.2).

An exact simultaneous distribution derivable at any thickness of t is solved based on the well-known model of screened single scattering under the fixed energy condition, which shows the Molière theory gives accurate and reliable distributions if the numerical integrations of inverse Fourier transforms are well converged within the accurate central region of spectrum in case of large enough t (subsect. 3.4), though both the exact and the Molière simultaneous distributions obtained here are valid under the small angle approximation and are applicable to charged particles not suffering radiation loss (subsect. 2.1).

The Molière simultaneous distribution, as easy to handle as the traditional angular distribution, will give more reliable and accurate results than the individual distribution in theoretical predictions and data analyses of experiments concerning charged particle transports, and will also give higher accuracy and efficiency in tracing charged particles in simulation works [29,30].

The authors wish to express their sincere gratitude to Dr. Naoya Takahashi for his contributions at the early stage of our investigations.

Appendix A. The dilogarithm function

The dilogarithm function is defined as

$$\begin{aligned}\mathrm{Li}_2(z) &\equiv -\int_0^z \frac{\ln(1-u)}{u}\,\mathrm{d}u \\ &= \sum_{k=1}^{\infty} z^k/k^2, \quad (-1 < z < 1) \end{aligned} \tag{A.1}$$

$$\mathrm{Li}_2(z) = -\,\mathrm{Li}_2\left(\frac{1}{z}\right) - \frac{\pi^2}{6} - \frac{1}{2}\ln^2(-z), \quad (z < -1) \tag{A.2}$$

$$\mathrm{Li}_2(z) = \mathrm{Li}_2(1) - \int_1^z \frac{\ln|1-u|}{u}\,\mathrm{d}u, \quad (1 < z) \tag{A.3}$$

$$\mathrm{Li}_2(-1) = -\pi^2/12, \quad \mathrm{Li}_2(1) = \pi^2/6. \tag{A.4}$$

References

1. G. Molière, Z. Naturforsch. **2a**, 133 (1947).
2. G. Molière, Z. Naturforsch. **3a**, 78 (1948).
3. H.A. Bethe, Phys. Rev. **89**, 1256 (1953).
4. T. Nakatsuka, J. Nishimura, Phys. Rev. E **78**, 021136 (2008).
5. G. Molière, Z. Naturforsch. **10a**, 177 (1955).
6. K. Kamata, J. Nishimura, Prog. Theor. Phys. Suppl. **6**, 93 (1958).
7. J. Nishimura, in *Handbuch der Physik, Band 46*, edited by S. Flügge (Springer, Berlin, 1967) Teil **2**, p. 1.
8. T. Nakatsuka, Phys. Rev. D **35**, 210 (1987).
9. P. Andreo, J. Medin, A.F. Bielajew, Med. Phys. **20**, 1315 (1993).
10. T. Nakatsuka, K. Okei, N. Takahashi, Nucl. Instrum. Methods Phys. Res. B **311**, 60 (2013).
11. H. Snyder, W.T. Scott, Phys. Rev. **76**, 220 (1949).
12. A.F. Bielajew, Nucl. Instrum. Methods Phys. Res. B **86**, 257 (1994).
13. W.T. Scott, Rev. Mod. Phys. **35**, 231 (1963).
14. A. Iyono, S. Yamamoto, H. Matsumoto, K. Okei, T. Nakatsuka, in *Proceedings of the 34th International Cosmic Ray Conference, Hague, 2015*, PoS (ICRC, 2015) 957, `http://pos.sissa.it/cgi-bin/reader/conf.cgi?confid=236`.
15. DONUT Collaboration (K. Kodama *et al.*), Phys. Lett. B **504**, 218 (2001).
16. M. De Serio *et al.*, Nucl. Instrum. Methods Phys. Res. A **512**, 539 (2003).
17. MACRO Collaboration (M. Ambrosio *et al.*), Phys. Lett. B **566**, 35 (2003).
18. MACRO Collaboration (M. Ambrosio *et al.*), Nucl. Instrum. Methods Phys. Res. A **492**, 376 (2002).
19. S. Aoki *et al.*, Nucl. Phys. B Proc. Suppl. **196**, 50 (2008).
20. MACRO Collaboration (M. Ambrosio *et al.*), Astrophys. J. **546**, 1038 (2001).
21. B. Rossi, K. Greisen, Rev. Mod. Phys. **27**, 240 (1941).
22. T. Nakatsuka, K. Kobayakawa, T. Kitamura, in *20th International Cosmic Ray Conference, Moscow, 1987, Conference Papers*, Vol. **6**, p. 261.
23. K. Okei, T. Nakatsuka, in *Proceedings of the Fourteenth EGS User's Meeting in Japan, KEK Proceedings 2007-5* (2007) 26.
24. L. Eyges, Phys. Rev. **74**, 1534 (1948).
25. S. Wolfram, *The Mathematica Book*, 4th edition (Cambridge University Press, Cambridge, UK, 1999).
26. T. Nakatsuka, Phys. Rev. D **58**, 056002 (1998).
27. K. Okei, N. Takahashi, T. Nakatsuka, in *30th International Cosmic Ray Conference, Merida, 2007, Conference Papers*, Vol. **4**, p. 157.
28. M. Abramowitz and I. A. Stegun (Editors), *Handbook of Mathematical Functions with Formulas, Graphs, and Mathematical Tables* (Dover, New York, 1965).
29. W.R. Nelson, H. Hirayama, D.W.O. Rogers, *The EGS4 Code System*, SLAC-265, Stanford Linear Accelerator Center (Dec. 1985).
30. GEANT4 Collaboration, Nucl. Instrum. Methods A **506**, 250 (2003).